

Properties of CeO₂ and Ce_{1-x}Zr_xO₂ Nanoparticles: X-ray Absorption Near-Edge Spectroscopy, Density Functional, and Time-Resolved X-ray Diffraction Studies

José A. Rodríguez,* Jonathan C. Hanson, Jae-Yong Kim, and Gang Liu

Department of Chemistry, Brookhaven National Laboratory, Upton, New York 11973

Ana Iglesias-Juez and Marcos Fernández-García*

Instituto de Catálisis y Petroleoquímica, CSIC, Campus Cantoblanco, 28049 Madrid, Spain

Received: October 28, 2002; In Final Form: December 20, 2002

In this article the structural and electronic properties of CeO₂ and Ce_{1-x}Zr_xO₂ nanoparticles are investigated using time-resolved X-ray diffraction, X-ray absorption near-edge spectroscopy (XANES), and density functional calculations. CeO₂ and Ce_{1-x}Zr_xO₂ ($x \leq 0.5$) particles in sizes between 4 and 7 nm were synthesized using a novel microemulsion method. The atoms in these nanoparticles adopted a cubic or pseudocubic crystal structure. The lattice constant decreased with increasing Zr content, varying from 5.4019 Å in CeO₂ to 5.3066 Å in Ce_{0.5}Zr_{0.5}O₂. Within the cubic structure, the Zr atoms exhibited structural perturbations that led to different types of Zr–O distances and nonequivalent O atoms in the Ce_{1-x}Zr_xO₂ compounds. Upon the addition of Zr to CeO₂, the Zr positive charge in Ce_{1-x}Zr_xO₂ is smaller than in pure ZrO₂ whereas the Ce positive charge is larger than in pure CeO₂. Combination of these geometrical and electronic effects produced Zr L_{III}-edge and O K-edge XANES spectra with a distinctive line-shape not seen in pure ZrO₂ or CeO₂. The doping with Zr increases the thermal stability of the ceria nanoparticles and their chemical reactivity toward hydrogen. At temperatures between 300 and 900 °C, the Ce_{1-x}Zr_xO₂ nanoparticles reacted with H₂ and water evolved into gas phase. XANES showed the generation of Ce³⁺ cations (without reduction of Zr⁴⁺) but an absence of diffraction lines different from fluorite-type ones was noted. There was an expansion in the unit cell of the reduced particles probably as a consequence of a partial Ce⁴⁺ → Ce³⁺ transformation and the sorption of hydrogen into the bulk of the material. The Ce_{1-x}Zr_xO₂ nanoparticles interact with H₂ and reduce at lower temperatures than bulk Ce_{1-x}Zr_xO₂ systems. This important difference could originate in an enhancement in chemical reactivity characteristic of nanostructured materials.

I. Introduction

Today, the protection of the environment is receiving much more attention than ever before. One of the major efforts of environmental cleanup is focused on controlling the emission of toxic pollutants produced during the combustion of fuels in automotive engines.^{1,2} The so-called three-way catalysts (TWC) are commonly used to reduce the emissions of CO, NO_x, and hydrocarbons from automobile exhaust.^{3,4} Due to its redox properties, ceria (CeO₂) is a key component in these catalysts.^{2,3,5} Ceria-supported noble-metal catalysts are capable of storing oxygen under oxidizing conditions and releasing oxygen under reducing conditions via the facile conversion between Ce⁴⁺ and Ce³⁺ oxidation states.⁵ Oxygen anion vacancies in ceria are considered to play an essential role in catalytic reactions.^{5–9} The energetics of O vacancy creation/filling can be altered after doping ceria with a second metal.^{10–12}

To enhance the redox properties and thermal stability of pure ceria, zirconia (ZrO₂) is often mixed as an additive to form solid solutions of the Ce_{1-x}Zr_xO₂ type ($x \leq 0.5$). For these materials, tetragonal and cubic structures are possible. Typically, cations are randomly distributed in a fluorite-type subcell, whereas the total symmetry is governed by the anion subcell.⁵ It can be, however, noted that cationic order is detected in some cubic phases.⁵ Mixed domains or regions, instead of solid solutions,

have also been reported for ceria–zirconia systems.¹⁰ All Zr-doped cerium mixed oxides (with x close to 0.5) enhance the oxygen storage capacity (OSC) as well as the rate for the oxygen release in automotive catalysts.^{10,13–15} They also retard thermal deactivation.^{2,10,13,14} The focus has been on examining possible correlations between the CeO₂ ↔ ZrO₂ interactions and differences in the behavior of Ce_{1-x}Zr_xO₂ and CeO₂. The mechanisms for the doping effects of Zr remain uncertain and are still a matter of debate. It has been suggested that ceria structural modifications mediated by zirconia^{13,14} and zirconia-stabilized defects in ceria^{10b} are responsible for the enhanced OSC properties of ceria–zirconia mixed oxides. Contributions from “electronic effects” (i.e., modifications in the chemical properties of the metal cations as a consequence of electronic perturbations) have been often dismissed, although it is clear that they cannot be ruled out.^{6,12,16}

New environmental regulations emphasize the importance of more efficient technologies for controlling and decreasing the emissions of CO, NO_x, and hydrocarbons in automotive engines.² This fact has motivated a strong interest in enhancing the catalytic properties of Ce_{1-x}Zr_xO₂ by preparing novel structures or spatial arrays of this material.^{4,15,17,18} In the emerging field of nanotechnology a goal is to make nanostructures with interesting functional properties. In principle, the chemical properties of a material can change when the “length scale” varies from a bulk sample to nanoparticles. Recent studies

* To whom correspondence should be addressed.

have shown that nanoparticles of $\text{Ce}_{1-x}\text{Zr}_x\text{O}_2$ can be prepared by a novel microemulsion method that leads to highly homogeneous materials in terms of chemical composition (i.e., Ce,Zr distribution), having a narrow distribution of particle sizes.^{15,17,19} The catalysts prepared in this way are very useful for studying the thermal stability of the $\text{Ce}_{1-x}\text{Zr}_x\text{O}_2$ system and aging treatments at high temperature.^{17,19} Oxygen handling and thermal stability properties of $\text{Ce}_{1-x}\text{Zr}_x\text{O}_2$ nanostructured materials primarily depend on structural parameters (phase-type) and chemical homogeneity (i.e., Ce,Zr distribution through the solid solution). Generally speaking, ordered cubic (κ) or disordered t' -tetragonal phases optimize redox properties^{5,20} and surface Ce enrichment may enhance oxygen handling but markedly decreases thermal stability.^{19,20} On the other hand, the general redox properties of Ce,Zr can vary with the size of an oxide particle.²⁰ This is grounded in the fact that all, surface and bulk, oxygen atoms are potentially involved in redox processes in a nanoparticle whereas in bulk ceria oxide, for example, only surface ones can be used.^{5,19,20}

In this article, the structural and electronic properties of $\text{Ce}_{1-x}\text{Zr}_x\text{O}_2$ nanoparticles are investigated using time-resolved X-ray diffraction (XRD),²¹ X-ray absorption near-edge spectroscopy (XANES),^{22,23} and density functional (DF) calculations.²⁴ Investigations at Brookhaven National Laboratory have established the feasibility of conducting subminute, time-resolved XRD experiments when the high intensity of synchrotron radiation and new parallel data-collection devices are combined.^{21a} This technique is ideal for studying structural transformations in $\text{Ce}_{1-x}\text{Zr}_x\text{O}_2$ nanoparticles as a function of temperature or reaction conditions. Here, H_2 chemisorption is used to study the chemical properties of the $\text{Ce}_{1-x}\text{Zr}_x\text{O}_2$ nanoparticles. The study has practical applications, as hydrogen is one of the reducing agents of exhaust gases⁵ and ceria-containing materials have the potential to form bronze-like phases, thus being hydrogen storage materials.²⁶ The deviation of bulk ceria from its ideal CeO_2 composition has been extensively studied by temperature-programmed reduction (TPR) with hydrogen.^{25–27} Experimental^{26,27a} and theoretical²⁵ studies indicate that hydrogen can be incorporated into bulk ceria, slightly expanding the lattice of the oxide. It is worthwhile to examine if the same phenomenon can occur in the $\text{Ce}_{1-x}\text{Zr}_x\text{O}_2$ nanoparticles and study the mechanism for the partial reduction of these systems.

II. Experimental Section and Theoretical Methods

II.1. Synthesis of the $\text{Ce}_{1-x}\text{Zr}_x\text{O}_2$ Nanoparticles. The nanoparticles of $\text{Ce}_{1-x}\text{Zr}_x\text{O}_2$ were prepared using an adaptation of the microemulsion method reported previously.^{15,17} Three specimens were prepared with initial Ce:Zr atomic ratios of 9:1, 2:1, and 1:1 in the reacting mixtures. The corresponding Ce(III) nitrate hexahydrate (Aldrich, purity 99.9%) and zirconyl nitrate (Aldrich, purity 99.99%) were introduced in a reverse microemulsion (water in oil) using *n*-heptane as the organic phase, Triton X-100 (Aldrich) as surfactant, and hexanol as cosurfactant. This suspension was mixed with another one (having similar characteristics in terms of the water/organic concentrations) containing as aqueous phase an alkali solution (TMAH, Aldrich). The resulting mixtures, with all cations coprecipitated, were stirred for 24 h, centrifuged, decanted, and rinsed with methanol. After the solid portion was dried overnight at 80 °C, the resulting powders were calcinated at 500 °C for 2 h. These materials will be hereafter referred to as $\text{Ce}_{0.9}\text{Zr}_{0.1}\text{O}_2$, $\text{Ce}_{0.66}\text{Zr}_{0.33}\text{O}_2$, and $\text{Ce}_{0.5}\text{Zr}_{0.5}\text{O}_2$ (in correlation with the corresponding atomic ratios). Chemical analysis (by ICP-AES) showed dif-

ferences of Ce:Zr atomic content within 10% of the nominal values. All binary oxides displayed a pseudocubic t'' -structure and BET specific areas of 142 ($\text{Ce}_{0.9}\text{Zr}_{0.1}\text{O}_2$), 152 ($\text{Ce}_{0.66}\text{Zr}_{0.33}\text{O}_2$), and 147 ($\text{Ce}_{0.5}\text{Zr}_{0.5}\text{O}_2$) $\text{m}^2 \text{g}^{-1}$. A ceria oxide fluorite-type reference was also synthesized ($S_{\text{BET}} = 122 \text{ m}^2 \text{g}^{-1}$).

II.2. Time-Resolved XRD Experiments. The time-resolved diffraction data were collected on beam line X7B of the National Synchrotron Light Source (NSLS).^{21a,28} In the experiments dealing with the thermal stability and sintering of the $\text{Ce}_{1-x}\text{Zr}_x\text{O}_2$ nanoparticles, the sample was kept in a quartz capillary and heated using a small resistance heater placed under the capillary.²¹ A chromel–alumel thermocouple was used to measure the temperature of the sample. In the experiments for the reduction with H_2 , samples of $\text{Ce}_{1-x}\text{Zr}_x\text{O}_2$ were loaded in an open sapphire capillary that was attached to a flow-reaction cell similar to those described in refs 29 and 30. The capillary was connected to $1/16$ in. Swagelok style fittings with Vespel ferrules. A 0.010 in. chromel–alumel thermocouple was inserted straight into the capillary near the oxide sample.²⁹ The oxide sample was heated using a small resistance heater wrapped around the capillary. Diffraction patterns were recorded at temperatures in the range 25–950 °C under a 5% H_2 /95% He gas mixture (flow rate = 5–15 cm^3/min). A MAR345 detector was used to record the in situ XRD data. The typical time required for collecting an individual diffraction pattern was in the range 0.5–2 min. The powder rings were integrated using the FIT2D code.³¹ Rietveld refinements were performed with the program GSAS³² in a manner similar to that followed in a previous work.^{33,34}

II.3. XANES Experiments. The Ce and Zr L_{III} -edge XANES spectra were collected at the NSLS on beam line X19A in the “fluorescence-yield mode” using a boomerang-type flat crystal monochromator and a special cell with a modified Stern–Heald–Lytle detector. Beamline U7A was utilized to record the O K-edge spectra. This beamline is equipped with a toroidal-spherical grating monochromator. The O K-edge spectra were taken in the “electron-yield mode” by using a channeltron multiplier located near the sample surface. The energy resolution at the Ce and Zr L_{III} -edges and the O K-edge was close to 0.5 eV. All the XANES spectra were taken at room temperature.

II.4. Theoretical Methods. The first-principles density functional (DF) calculations reported in section III were performed using the CASTEP (Cambridge Serial Total Energy Package) suite of programs.^{24,35} In this code, the Kohn–Sham implementation of DF theory is used to obtain the total energy of the system. CASTEP has an excellent track record in accurate prediction of geometry and energetics for oxide systems.^{6,35–40} In this code, the wave functions of valence electrons are expanded in a plane wave basis set with k -vectors within a specified energy cutoff E_{cut} . Tightly bound core electrons are represented by nonlocal ultrasoft pseudopotentials.⁴¹ Brillouin Zone integration is approximated by a sum over special k -points chosen using the Monkhorst–Pack scheme.⁴² In all the calculations, the kinetic energy cutoff E_{cut} (400 eV), and the density of the Monkhorst–Pack k -point mesh (a $4 \times 4 \times 4$ grid in the smallest unit cells, reduced to a $4 \times 4 \times 2$ grid for larger cells) were chosen high enough to ensure convergence of the computed structures and energetics. The exchange–correlation contribution to the total electronic energy was treated in a generalized-gradient corrected (GGA) form of the local density approximation (LDA): Perdew–Burke–Ernzerhoff functional.⁴³ The structural parameters of the bulk CeO_2 and $\text{Ce}_{1-x}\text{Zr}_x\text{O}_2$ systems in their different configurations were determined using the Broyden–Fletcher–Goldfarb–Shanno (BFGS) minimization technique, with the following thresholds for the converged

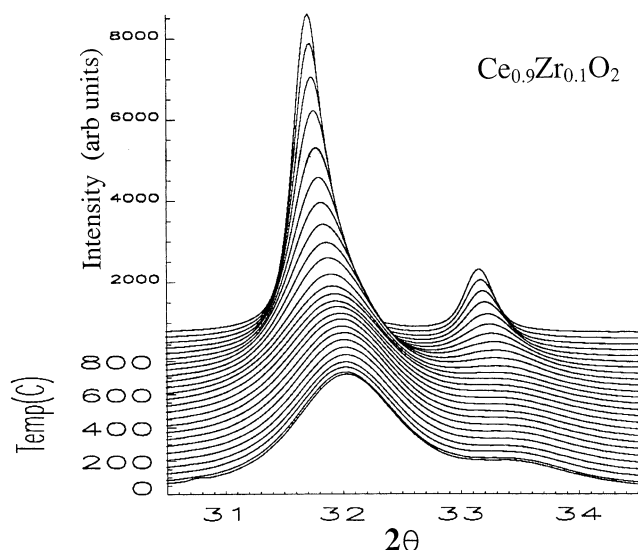


Figure 1. Time-resolved XRD data for the heating of Ce_{0.9}Zr_{0.1}O₂ nanoparticles in air. Heating rate = 4.8 °C/min. $\lambda = 0.8941$ Å.

structures: energy change per atom less than 5×10^{-6} eV, residual force less than 0.02 eV/Å, displacement of atoms during the geometry optimization less than 0.001 Å, and root mean square (rms) of the stress tensor less than 0.1 GPa. For each optimized structure, the partial charges on the atoms were estimated by projecting the occupied one-electron eigenstates onto a localized basis set with a subsequent Mulliken population analysis.^{44,45} Mulliken charges have well-known limitations,⁴⁶ but are nevertheless useful as a qualitative tool to study trends in charge distribution.

III. Results

III.1. Structural Properties and Sintering of Ce_{1-x}Zr_xO₂ Nanoparticles. Figure 1 shows time-resolved XRD results obtained after heating a sample of Ce_{0.9}Zr_{0.1}O₂ nanoparticles from 25 to 900 °C. Similar results were found for other Ce_{1-x}Zr_xO₂ systems. When the temperature is raised, the diffraction lines clearly gain intensity and become better defined. No phase transformation is visible. These changes are a consequence of an increase in the size of the particles (sintering) at temperatures above 500 °C. This process is irreversible.

From the width of the diffraction lines one can get a reasonable estimate of the average size of the CeO₂ and Ce_{1-x}Zr_xO₂ nanoparticles.⁴⁷ Figure 2 displays changes in size as a function of temperature. Initially, the particles have a size in the range 4–7 nm. The size of the pure CeO₂ nanoparticles (~7 nm) is comparable to that obtained recently using a different synthetic method.¹⁸ Around 600 °C, the size of the particles starts to increase and by 900 °C is close to 18 nm. For the Ce_{1-x}Zr_xO₂ systems the sintering also starts near 600 °C, but the magnitude of the size increase diminishes when the content of Zr is raised. The Ce_{0.5}Zr_{0.5}O₂ nanoparticles exhibit the highest thermal stability, and their size increases by only 2.5 nm when the temperature increases from 500 to 950 °C. In this case, the “extra” thermal stability could be consequence of a more dense packing of the atoms in the unit cell of the compound, as we will see below. The trends in Figure 2 are important and consistent with the fact that the addition of zirconia to ceria enhances the thermal stability of automotive catalysts.^{2,10,13,14}

Table 1 lists lattice constants determined from a Rietveld refinement of our XRD data for the CeO₂ and Ce_{1-x}Zr_xO₂ nanoparticles. The small size of these systems puts a limit in

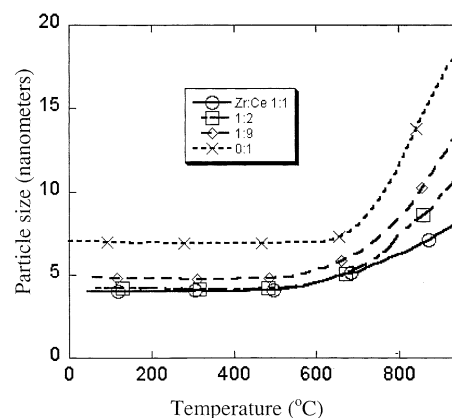


Figure 2. Effects of heating on the size of a series of Ce_{1-x}Zr_xO₂ ($x = 0, 0.1, 0.33, 0.5$) nanoparticles.

TABLE 1: Lattice Constant (a) for CeO₂ and Ce_{1-x}Zr_xO₂

	a nanoparticles, XRD data (Å)	a bulk, DF results (Å)
CeO ₂	5.4019	5.46 (5.4108) ^a
Ce _{0.9} Zr _{0.1} O ₂	5.3984	
Ce _{0.875} Zr _{0.125} O ₂		5.44
Ce _{0.75} Zr _{0.25} O ₂		5.39
Ce _{0.66} Zr _{0.33} O ₂	5.3573	
Ce _{0.5} Zr _{0.5} O ₂	5.3066	5.30
Ce _{0.25} Zr _{0.75} O ₂		5.17
Ce _{0.125} Zr _{0.875} O ₂		5.15
ZrO ₂		5.11

^a XRD value for bulk CeO₂.

the accuracy of our structural analysis, and the a parameter listed in some cases in fact represents an average value for a pseudocubic phase with a slight tetragonal distortion. For comparison, we also include in Table 1 lattice constants calculated with DF for bulk CeO₂ and Ce_{1-x}Zr_xO₂ in a cubic structure. In the experimental and theoretical results, one can see the same trend: as the content of Zr increases, there is a reduction in the lattice constant of the oxide. For $x < 0.5$, the lattice parameter displays a linear relationship with Zr content of the mixed oxide.^{5b,48} An identical result has been found in XRD studies for bulk Ce_{1-x}Zr_xO₂^{5b,48} although the slope of the linear relationship has been shown to be dependent on particle size.^{5b} The lattice constant decrease is a consequence of the smaller size of Zr with respect to Ce.^{20b,49} The DF calculations indicate that this difference in size is quite important for the local structure of the metal cations. Even within a cubic structure, the Zr atoms exhibit a structural perturbation that leads to different types of Zr–O distances and nonequivalent O atoms in the Ce_{1-x}Zr_xO₂ compounds. In essence, it is very difficult for the Zr atoms to adopt the large metal–oxygen distances expected in a lattice of CeO₂. The perturbations in the Zr–O coordination sphere could be responsible for the high oxygen mobility seen in ceria–zirconia mixed oxides.^{20b,48}

Figure 3 shows how the unit cell parameter of the CeO₂ and Ce_{1-x}Zr_xO₂ nanoparticles changes as a function of temperature. The results for bulk CeO₂ and the CeO₂ nanoparticles are close, showing a continuous expansion of the unit cell from 25 to 950 °C. Something similar is observed for the nanoparticles independently of the content of Zr. In the nanoparticles the cell expansion at temperatures above 600 °C is accompanied by sintering (Figure 2). Comparison of the slopes of the curves in Figures 2 and 3 seems to indicate that the sintering process does not have a major effect in the unit cell expansion of the

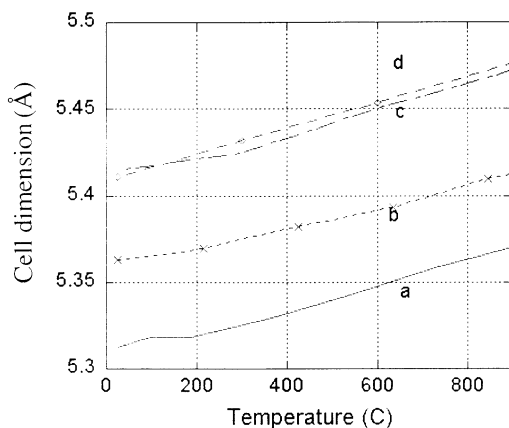


Figure 3. Cell dimension as a function of temperature for a series of nanoparticles: (a) $\text{Ce}_{0.5}\text{Zr}_{0.5}\text{O}_2$; (b) $\text{Ce}_{0.66}\text{Zr}_{0.33}\text{O}_2$; (c) $\text{Ce}_{0.90}\text{Zr}_{0.10}\text{O}_2$; (d) CeO_2 .

nanoparticles. This expansion is probably a direct result of an increase in temperature (i.e., thermal movement of the atoms within the unit cell).

III.2. Electronic Properties of the $\text{Ce}_{1-x}\text{Zr}_x\text{O}_2$ Nanoparticles. The electronic properties of the $\text{Ce}_{1-x}\text{Zr}_x\text{O}_2$ nanoparticles were investigated using XANES and DF calculations. XANES measurements were done at the Ce and Zr L_{III} -edges and at the O K-edge. The spectra for the Ce L_{III} -edge of the nanoparticles showed energies and the line shape reported for bulk CeO_2 .^{23,50} Thus, the limited size of these systems or the doping with Zr did not induce formation of a significant amount of Ce^{3+} . Figure 4 shows Zr L_{III} -edge spectra for bulk ZrO_2 and $\text{Ce}_{1-x}\text{Zr}_x\text{O}_2$ nanoparticles. At the temperature at which the spectra were acquired (~ 300 K), a monoclinic crystal structure is the thermodynamically stable phase for ZrO_2 .^{6,51} The Zr L_{III} -edge of this oxide is characterized by four distinctive features. The two main ones (a, b) correspond to electronic transitions from the occupied Zr 2p orbitals to the empty Zr 4d orbitals, which are split into orbitals with t and e symmetry.⁵² In oxides, the relative intensity of the a and b peaks depends strongly on the chemical environment around the Zr cations.⁵² In the $\text{Ce}_{1-x}\text{Zr}_x\text{O}_2$ nanoparticles, the Zr atoms are in a pseudocubic environment and the relative intensity of the b peak is stronger than that observed for monoclinic ZrO_2 or for tetragonal Zr-doped Y_2O_3 .⁵² The a–b peak separation in $\text{Ce}_{0.9}\text{Zr}_{0.1}\text{O}_2$ is ~ 0.25 eV larger than that in ZrO_2 . As the concentration of zirconium in $\text{Ce}_{1-x}\text{Zr}_x\text{O}_2$ increases, the Zr L_{III} -edge line shape changes and becomes closer to that in pure ZrO_2 (bottom of Figure 4).

Figure 5 displays O K-edge XANES spectra for a series of $\text{Ce}_{1-x}\text{Zr}_x\text{O}_2$ nanoparticles, including reference spectra for bulk ZrO_2 and CeO_2 . The features labeled 4f, 5d– e_g , and 5d– t_{2g} in pure CeO_2 are related to electronic transitions from the O 1s core levels to the empty cerium 4f, 5d e_g , and 5d t_{2g} levels, respectively.⁵³ The O K-edge spectrum of ZrO_2 comes mainly from O 1s \rightarrow Zr(4d) electronic transitions,^{6,22} and the two main peaks reflect the splitting of the Zr 4d orbitals into levels with e_g and t_{2g} symmetry.⁵² The O K-edge spectra of the $\text{Ce}_{1-x}\text{Zr}_x\text{O}_2$ nanoparticles significantly change as a function of Zr doping. They exhibit features that match very well those found previously for bulklike films of $\text{Ce}_{1-x}\text{Zr}_x\text{O}_2$.⁶ The O K-edge spectra of $\text{Ce}_{1-x}\text{Zr}_x\text{O}_2$ compounds have a distinctive line shape that cannot be attributed to a sum of CeO_2 and ZrO_2 peaks. This is consistent with the results of our DF calculations, which show Ce–O and Zr–O bond distances in $\text{Ce}_{1-x}\text{Zr}_x\text{O}_2$ not seen in the isolated oxides (i.e., some O atoms are in a special chemical environment).

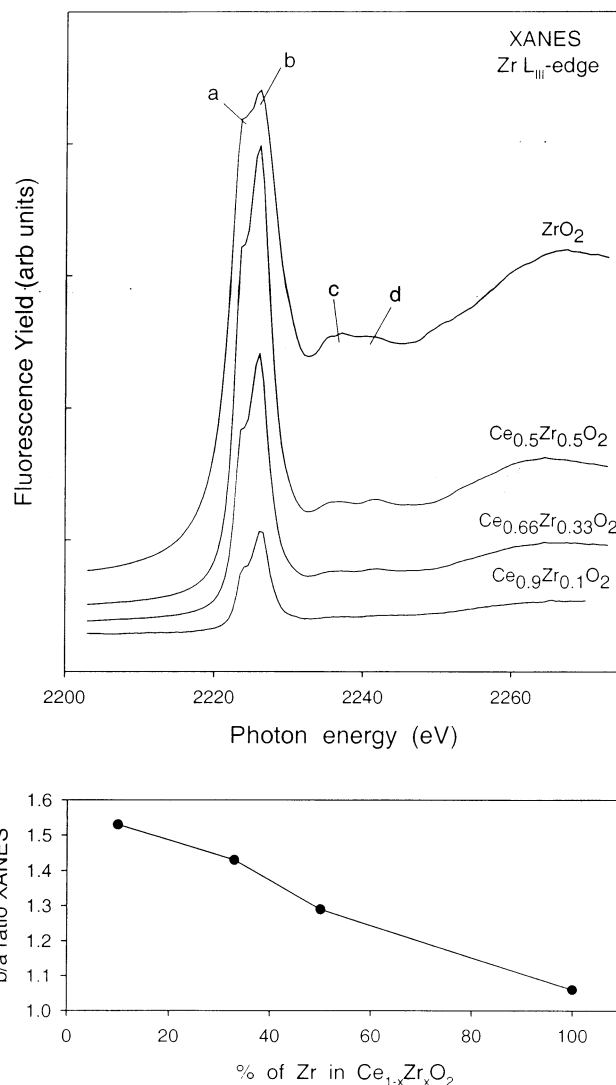


Figure 4. Zr L_{III} -edge XANES spectra for bulk ZrO_2 and $\text{Ce}_{1-x}\text{Zr}_x\text{O}_2$ nanoparticles.

Using DF calculations, we investigated the charge distribution in bulk $\text{Ce}_{1-x}\text{Zr}_x\text{O}_2$ and small stoichiometric clusters. In agreement with early studies,^{6,51,54–56} our calculations indicate that bulk CeO_2 and ZrO_2 are far from being fully ionic compounds. This is valid independent of the method of calculation and the type of basis set used to describe the atomic orbitals of Zr, Ce and O.^{6,51,55,56} In the valence bands of ceria and zirconia there is a very significant amount of metal character. Upon the addition of Zr to CeO_2 , we found that in $\text{Ce}_{1-x}\text{Zr}_x\text{O}_2$ the positive charge on Zr is smaller than in pure ZrO_2 , whereas the positive charge on Ce is larger than in pure CeO_2 . This is illustrated in the results of Figure 6 for bulk $\text{Ce}_{1-x}\text{Zr}_x\text{O}_2$ in a cubic structure and was also found in DF calculations after replacing Ce with Zr in the clusters of Figure 7. Interestingly, when Zr replaces Ce in bulk ceria or Ce_nO_{2n} clusters, the Zr–O distances obtained are larger than in the corresponding ZrO_2 systems, and at the same time the Ce–O distances become shorter than in the initial CeO_2 compounds. The variations in cation charge seen in the bulk compounds (Figure 6) and small clusters track changes in cation–oxygen distances: the larger the metal–oxygen bond length, the smaller the charge in the cation.

Returning to the Zr L_{III} -edge XANES spectra in Figure 4, it is likely that the changing line shape as a function of Zr

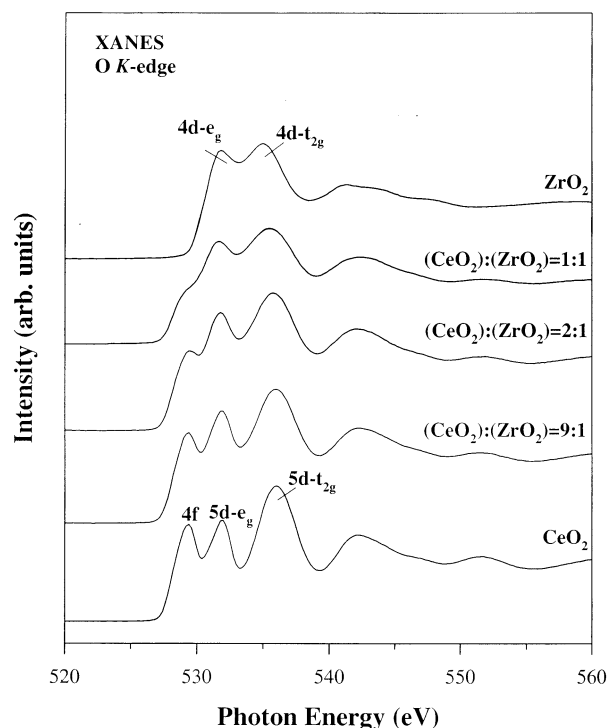


Figure 5. O K-edge XANES spectra for bulk ZrO₂, Ce_{1-x}Zr_xO₂ nanoparticles, and bulk CeO₂.

concentration is accompanied by perturbations in the occupancy of the Zr 4d orbitals and in the arrangement of the O atoms around the Zr cations. Corresponding changes in Ce-cation charges seem less influential in the Ce L_{III}-edge, probably due to energy resolution problems and the always large concentration of Ce in the samples. The O K-edge (Figure 5), however, suggests a modest stabilization of Ce orbitals (clearly visible for the 4f resonance in the Ce_{0.5}Zr_{0.5}O₂ sample). As the continuum resonances have an inverse dependence with the square of the coordination distance,²³ this shift has an electronic ground, as is likely induced by the larger positive charge detected for cerium cations in the Ce,Zr mixed oxides with respect to ceria. Crystal field effects appear of lesser importance when these two oxide types are compared, as the *e_g/t_{2g}* energy separation seems poorly sensitive to the Zr content of the material.

III.3. Reaction of the Ce_{1-x}Zr_xO₂ Nanoparticles with Hydrogen. In many situations oxide catalysts are activated by partial reduction in hydrogen.⁵⁷ Hydrogen is one of the reducing agents in automotive exhaust gases.⁵ The deviation of bulk ceria from its ideal CeO₂ composition has been extensively studied by temperature-programmed reduction (TPR) with hydrogen.²⁵⁻²⁷ Similar experiments have also been carried out for bulk Ce_{1-x}Zr_xO₂.^{20,48,58} We investigated the partial reduction of the Ce_{1-x}Zr_xO₂ nanoparticles using time-resolved XRD and XANES. Figure 8 shows diffraction patterns obtained after heating Ce_{0.9}-Zr_{0.1}O₂ nanoparticles from 25 to 900 °C under a 5% H₂/95% He stream (20 cm³/min). As the temperature increases, there is a narrowing of the diffraction peaks together with a clear shift in position. The narrowing indicates sintering of the nanoparticles (see above) and the shift to the lower angle in 2θ is a consequence of an expansion in their unit cell as a result of introducing O vacancies and/or sorbing hydrogen during the reduction process (see below). Similar trends were observed in the corresponding XRD data for nanoparticles of CeO₂, Ce_{0.5}-Zr_{0.5}O₂, and Ce_{0.66}Zr_{0.33}O₂. The diffraction results did not show

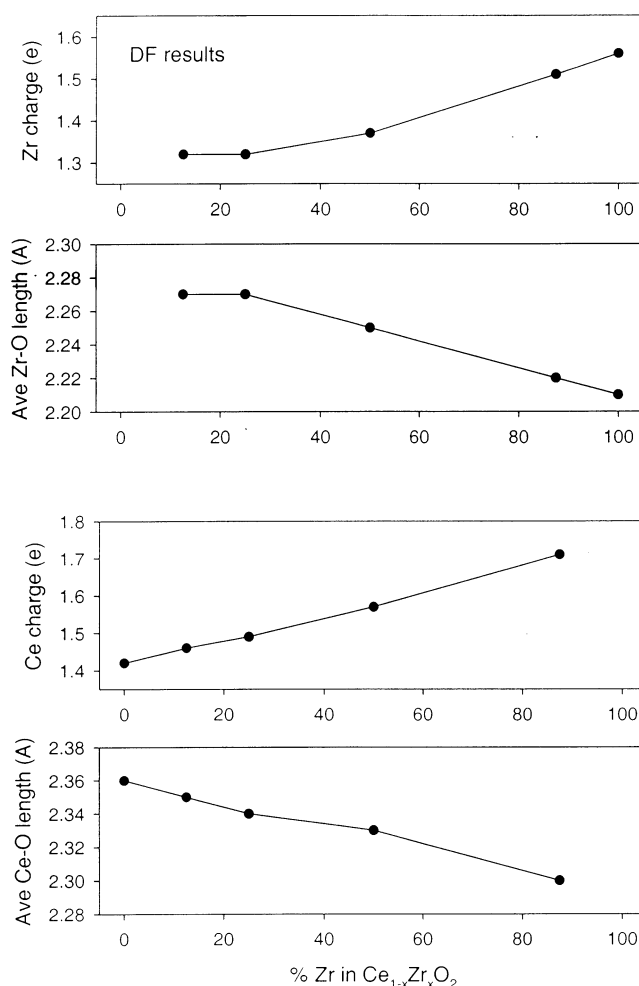


Figure 6. DF results for bulk Ce_{1-x}Zr_xO₂ in a cubic structure. The two top panels show the calculated Zr charge and average Zr–O bond length. The bottom two panels display the calculated Ce charge and the average Ce–O bond length.

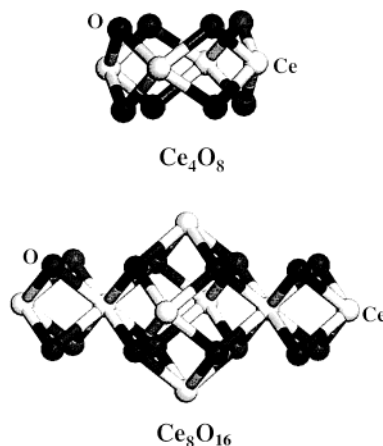


Figure 7. Ce₂O₄ and Ce₈O₁₆ clusters investigated in the DF calculations. Ce atoms (white spheres) were replaced with Zr to generate compounds with Ce_{1-x}Zr_xO₂ stoichiometry.

the formation of reduced oxides with the crystal structures of CeO_{1.71},⁵⁹ Ce₂O₃,⁶⁰ or Ce₂Zr₂O_{7+x} pyrochlore structures.^{5b,20b}

Figure 9 shows data for the isothermal reduction of Ce_{0.9}-Zr_{0.1}O₂ at 525 °C. In the first 20 min, the temperature of the sample was ramped from 25 to 525 °C. This produced an expansion in the unit cell of the nanoparticles. Then, the sample was exposed to a 5% H₂–95% He stream. Water evolution was

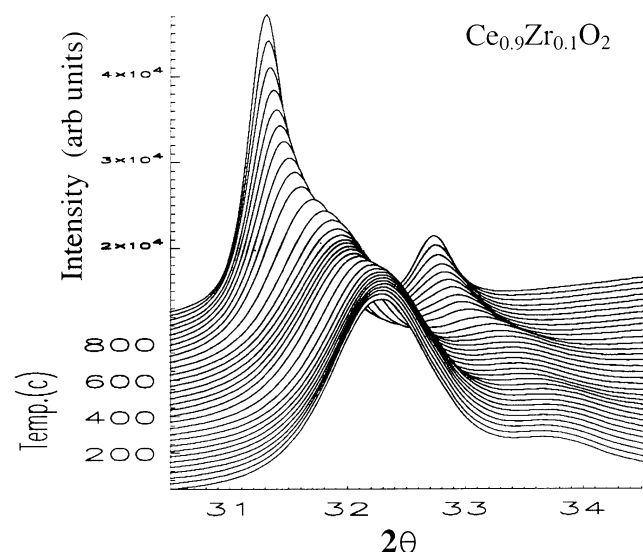


Figure 8. Time-resolved XRD data for the heating of $\text{Ce}_{0.9}\text{Zr}_{0.1}\text{O}_2$ nanoparticles under a flow of 5% H_2 –95% He. Heating rate = 5.9 °C/min. $\lambda = 0.9034$ Å.

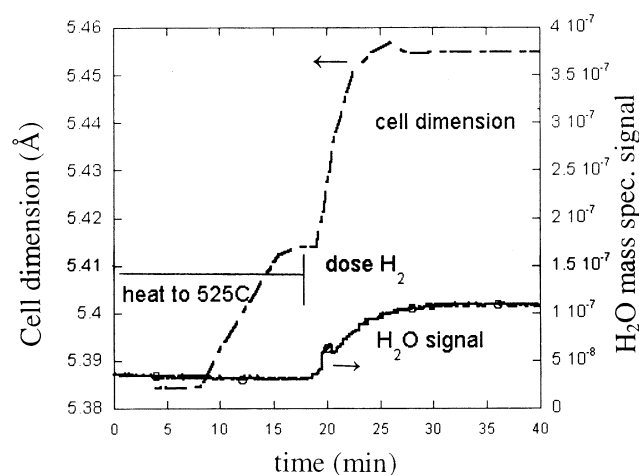


Figure 9. Data for the isothermal reduction of $\text{Ce}_{0.9}\text{Zr}_{0.1}\text{O}_2$ at 525 °C. In the first 20 min, the temperature of the sample was ramped from 25 to 525 °C. Then, the sample was exposed to a 5% H_2 –95% He stream. The left axis shows the variation in the unit cell parameter (a , Å) and corresponds to the dashed curve. The right axis displays the measured intensity for the water signal in a mass spectrometer and corresponds to the solid curve.

observed with a mass spectrometer located at the exit of the reaction cell and this was accompanied by an additional expansion of the unit cell. In similar experiments, XANES measurements at the Ce L_{III}-edge gave spectra with the line shape expected for a mixture of Ce^{4+} and Ce^{3+} .^{23,50,58} On the other hand, there were relatively minor changes in the Zr L_{III}-edge spectrum with respect to the fully oxidized sample. This is consistent with previous studies for bulk $\text{Ce}_{1-x}\text{Zr}_x\text{O}_2$ systems,^{6,61} which show that it is easier to reduce Ce^{4+} than Zr^{4+} in the mixed oxide. Thus, the expansion in the unit cell seen in Figures 8 and 9 probably reflects a change in the cation size when going from Ce^{4+} (small size) to Ce^{3+} (larger size).^{6,20b,60} Sorption of hydrogen into the nanoparticles also could contribute to enlarge the unit cell size.^{25,26,27a} Using DF calculations and following previous studies for bulk CeO_2 ,²⁵ we investigated the effects of one hydrogen atom placed inside the main cavity of the crystal structures of $\text{Ce}_{0.5}\text{Zr}_{0.5}\text{O}_2$ and $\text{Ce}_{0.75}\text{Zr}_{0.25}\text{O}_2$ with overall stoichiometries of $\text{H}_{0.25}\text{Ce}(\text{Zr})\text{O}_2$ and $\text{H}_{0.125}\text{Ce}(\text{Zr})\text{O}_2$ (Figure 10). The H did not remain at the high-symmetry position

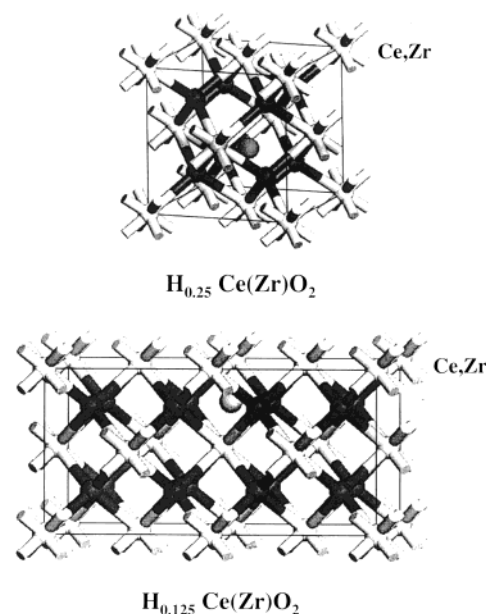


Figure 10. Unit cells used in DF calculations for $\text{H}_{0.25}\text{Ce}(\text{Zr})\text{O}_2$ and $\text{H}_{0.125}\text{Ce}(\text{Zr})\text{O}_2$ systems. The ratio of Ce/Zr varied from CeO_2 to $\text{Ce}_{0.75}\text{Zr}_{0.25}\text{O}_2$, and finally to $\text{Ce}_{0.5}\text{Zr}_{0.5}\text{O}_2$. White spheres represent Ce or Zr atoms. Dark spheres correspond to O atoms. The small gray spheres denote H atoms.

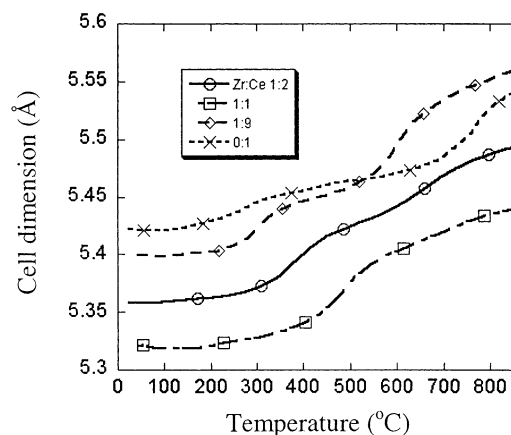


Figure 11. Variations in cell dimension (Å) during the H_2 -TPR of a series of nanoparticles: $\text{Ce}_{0.5}\text{Zr}_{0.5}\text{O}_2$ (\square symbols), $\text{Ce}_{0.66}\text{Zr}_{0.33}\text{O}_2$ (\circ), $\text{Ce}_{0.90}\text{Zr}_{0.10}\text{O}_2$ (\diamond), and CeO_2 (\times). The samples were heated under a flow (20 cm^3/min) of a 5% H_2 –95% He mixture. Heating rate ~ 6 °C/min.

in the center of a cavity, instead preferring to interact with O centers, forming hydroxyl species. These species can be seen as the precursors for the removal of O during the reduction process. In the case of systems with $\text{H}_{0.5}\text{Ce}(\text{Zr})\text{O}_2$ stoichiometry (two hydrogens inside a cavity), sorbed atomic H was energetically unstable and transformed into H_2 molecules. Table 2 shows the calculated lattice constants for the systems in Figure 10. The sorption of H produced an unit-cell expansion of 0.4–0.7% for a $\text{H}_{0.125}\text{Ce}(\text{Zr})\text{O}_2$ stoichiometry, and 1–1.6% at a $\text{H}_{0.25}\text{Ce}(\text{Zr})\text{O}_2$ stoichiometry. Thus, in the experiments of Figure 9 the concentration of H inside the nanoparticles is probably less than expected for a $\text{H}_{0.25}\text{Ce}(\text{Zr})\text{O}_2$ stoichiometry.

Figure 11 shows how the size of the unit cell of $\text{Ce}_{1-x}\text{Zr}_x\text{O}_2$ nanoparticles changes as a function of temperature when they are reduced in hydrogen. The cell expansions are much larger than seen during simple heating (compare to Figure 3) as a consequence of a chemical reaction (Ce^{3+} formation) and the sorption of hydrogen. The OSC of $\text{Ce}_{1-x}\text{Zr}_x\text{O}_2$ is clearly related

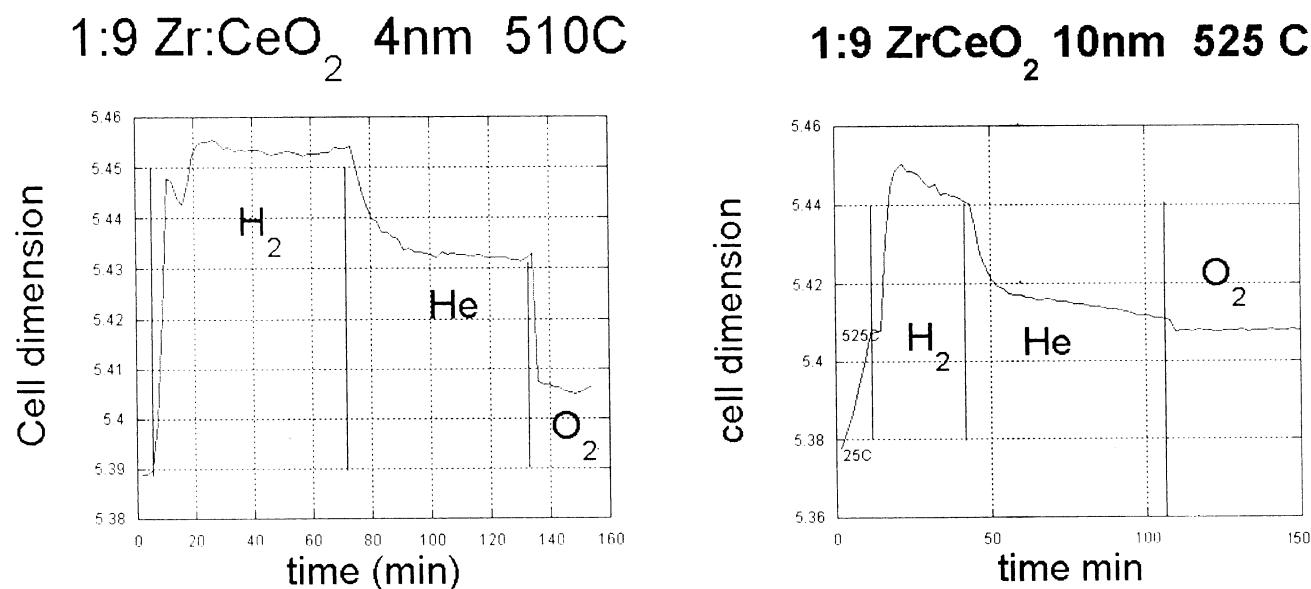


Figure 12. Left panel: XRD data for the partial reduction and reoxidation of 4 nm Ce_{0.9}Zr_{0.1}O₂. The nanoparticles were exposed to a mixture of 5% H₂–95% He at 25 °C and then heated at 510 °C. Subsequently, the hydrogen was replaced with a mixture of mainly He plus some O₂, and finally the He was replaced with pure O₂. Right panel: XRD data for the partial reduction and reoxidation of 10 nm Ce_{0.9}Zr_{0.1}O₂. The sample was first heated to 525 °C and then exposed to a stream of 5% H₂–95% He for 40 min. After partial reduction, H₂ was replaced with He/O₂ and pure O₂.

TABLE 2: Sorption of Hydrogen, Calculated Lattice Constants (a)^a

	without H (Å)	with H (Å)	
		H _{0.125} Ce(Zr)O ₂	H _{0.25} Ce(Zr)O ₂
CeO ₂	5.46	5.48	5.52
Ce _{0.75} Zr _{0.25} O ₂	5.39	5.42	5.47
Ce _{0.5} Zr _{0.5} O ₂	5.30	5.34	5.38

^a Cubic structures.

to the ratio of Ce/Zr.^{10,13–15,20} The magnitude of the changes in the lattice constant for the Ce_{1-x}Zr_xO₂ nanoparticles during reduction also depends on the Ce/Zr ratio. In Figure 11, similar trends are observed for the Ce_{0.9}Zr_{0.1}O₂, Ce_{0.66}Zr_{0.33}O₂, and Ce_{0.5}Zr_{0.5}O₂ systems. Substantial increases in cell dimension occur from 300 to 500 °C, and from 600 to 900 °C. The nanoparticles of CeO₂ have a different behavior: there is a minor cell expansion between 200 and 600 °C, and a rapid increase above 700 °C. It can be noted, however, that the Ce_{0.9}Zr_{0.1}O₂ material shows the two mentioned, well-defined regions of cell dimension variation, but only one abrupt jump followed by a smooth increase is detected for Ce_{0.5}Zr_{0.5}O₂. This can be rationalized by considering that, in ceria, surface and bulk oxygen mobility are well-differentiated processes whereas in the Ce_{0.5}Zr_{0.5}O₂ mixed oxide cannot be distinguished.^{5b,20} These results indicate that the variation from a ceria-like behavior to a ceria–zirconia is progressive, although very significant changes are already observed in terms of initial temperature (e.g., energy) when only 10% of Ce atoms are substituted by Zr.

On the other hand, it is clear that the CeO₂ nanoparticles exhibit the lowest reactivity in Figure 11. This agrees with trends found in H₂-TPR experiments for bulk CeO₂ and Ce_{1-x}Zr_xO₂,^{20a,48} and it is frequently linked to the OSC improvement seen in Zr-doped ceria.^{20,62} During the oxygen release process, there is stress in the oxide lattice as a consequence of the difference in atomic size of Ce⁴⁺ (0.97 Å) and Ce³⁺ (1.14 Å).^{20b} The introduction of relatively small Zr⁴⁺ ions (0.84 Å) into the ceria framework could compensate the volume increment, and ease the valence change (Ce⁴⁺ → Ce³⁺) and reduction process in Ce_{1-x}Zr_xO₂.^{20b,62} Interestingly, the Ce_{1-x}Zr_xO₂ nanoparticles in

Figure 11 start to reduce at lower temperatures than bulk Ce_{1-x}Zr_xO₂ systems (>400 °C).^{20a,48} This important difference could originate in an enhancement in chemical reactivity due to differences in the cation–anion energetics, attributable to the nanostructured properties of the materials.

Ceria-supported noble-metal catalysts release oxygen under reducing conditions and are capable to store oxygen under oxidizing conditions.⁵ We carried out studies of reduction/oxidation for the CeO₂ and Ce_{1-x}Zr_xO₂ nanoparticles. These studies revealed that the full reoxidation of partially reduced nanoparticles is possible at lower temperatures than those reported for the full reoxidation of bulk ceria.²⁰ Figure 12 displays XRD data for a fresh Ce_{0.9}Zr_{0.1}O₂ system (4 nm particle size, left panel) and a Ce_{0.9}Zr_{0.1}O₂ system preannealed to 950 °C (10 nm particle size, right panel). The 4 nm particles were exposed to a mixture of 5% H₂–95% He at 25 °C and then heated at 510 °C. This induced oxide reduction with an expansion in the unit cell. Subsequently, the hydrogen was replaced with a mixture of mainly He plus some O₂ (<1%), and finally the He was replaced with pure O₂. The last two steps lead to a contraction in the oxide unit cell due to the flushing of the sorbed hydrogen and the reoxidation of Ce³⁺. At the end, the system had a unit cell dimension close to that observed for 4 nm Ce_{0.9}Zr_{0.1}O₂ at 510 °C. In the experiment for the 10 nm particles, the sample was first heated to 525 °C and then exposed to a stream of 5% H₂–95% He for 40 min. After partial reduction, H₂ was replaced with He and a trace of O₂ (<1%), and then pure O₂, which led to almost full reoxidation. To do experiments similar to those seen in Figure 12 for bulk CeO₂, one needs temperatures much higher than 510–525 °C to obtain a significant reduction (cell expansion) and subsequent full reoxidation.^{20,48} Again, the higher chemical reactivity of the CeO₂ and Ce_{1-x}Zr_xO₂ nanoparticles could come from differences in the cation–anion energetics attributable to the nanostructured properties of the materials.

IV. Summary and Conclusions

In this article the structural and electronic properties of CeO₂ and Ce_{1-x}Zr_xO₂ nanoparticles were investigated using time-

resolved XRD, XANES, and DF calculations. CeO_2 and $\text{Ce}_{1-x}\text{Zr}_x\text{O}_2$ ($x \leq 0.5$) particles in sizes between 4 and 7 nm were synthesized using a novel microemulsion method. The atoms in these nanoparticles were arranged in a cubic or pseudocubic crystal structure. The lattice constant decreased with increasing Zr content, varying from 5.4019 Å in CeO_2 to 5.3066 Å in $\text{Ce}_{0.5}\text{Zr}_{0.5}\text{O}_2$. Within the cubic structure, the Zr atoms exhibited structural perturbations that led to different types of Zr–O distances and nonequivalent oxygen atoms in the $\text{Ce}_{1-x}\text{Zr}_x\text{O}_2$ compounds. Upon the addition of Zr to CeO_2 , the Zr positive charge in $\text{Ce}_{1-x}\text{Zr}_x\text{O}_2$ was smaller than in pure ZrO_2 whereas the Ce positive charge was larger than in pure CeO_2 . The variations in cation charge track changes in cation–oxygen distances: the larger the metal–oxygen bond length, the smaller the charge in the cation. The combination of structural (metal–oxygen distance) and electronic (mainly cation charge) effects produced Zr L_{III}-edge and O K-edge XANES spectra with a distinctive line shape not seen in pure ZrO_2 or CeO_2 .

The doping with Zr increased the thermal stability of the ceria nanoparticles (reducing sintering above 600 °C) and their chemical reactivity toward hydrogen. At temperatures between 300 and 900 °C, the $\text{Ce}_{1-x}\text{Zr}_x\text{O}_2$ nanoparticles reacted with H_2 and water evolved into the gas phase. A smooth evolution was observed with Zr content in the $\text{Ce}_{1-x}\text{Zr}_x\text{O}_2$ reduction behavior in going from the two-step (surface and bulk) mechanism characteristic of ceria to a single step typical of binary systems with a Ce/Zr atomic ratio close to 1. XANES showed the generation of Ce^{3+} cations (without reduction of Zr^{4+}) but no diffraction lines were detected for the formation of crystal structures similar to bulk $\text{CeO}_{1.71}$ or Ce_2O_3 . There was an expansion in the unit cell of the reduced particles probably as a consequence of a partial $\text{Ce}^{4+} \rightarrow \text{Ce}^{3+}$ transformation and the sorption of hydrogen. Hydrogen could be stored at the bulk of the mixed oxides with a H/cation ratio close to 0.2. The $\text{Ce}_{1-x}\text{Zr}_x\text{O}_2$ nanoparticles interact with H_2 and get reduced at lower temperatures than bulk $\text{Ce}_{1-x}\text{Zr}_x\text{O}_2$ systems. This important difference could originate in an enhancement in chemical reactivity due to differences in cation–anion energetics, attributable to the nanostructured properties of the materials.

Acknowledgment. The research carried out at the Chemistry Department of Brookhaven National Laboratory was financed through contract DE-AC02-98CH10086 with the U.S. Department of Energy (Division of Chemical Sciences). The NSLS is supported by the Divisions of Materials and Chemical Sciences of DOE. Work at the “Instituto de Catálisis (CSIC)” was done with financial support from CICYT (project MAT2000-1467).

References and Notes

- (1) Thomas, J. M.; Thomas, W. J. *Principles and Practice of Heterogeneous Catalysis*; VCH: New York, 1997.
- (2) Shelef, M.; McCabe, R. W. *Catal. Today* **2000**, 62, 35.
- (3) (a) Taylor, K. C. *Catal. Rev. Sci. Eng.* **1993**, 35, 457. (b) Shelef, M.; Graham, G. W. *Catal. Rev. Sci. Eng.* **1994**, 36, 433.
- (4) (a) Fernández-García, M.; Martínez-Arias, A.; Iglesias-Juez, A.; Hungria, A. B.; Anderson, J. A.; Conesa, J. C.; Soria, J. *Applied Catal. B: Environ.* **2001**, 31, 39. (b) Fernández-García, M.; Martínez-Arias, A.; Belver, C.; Anderson, J. A.; Conesa, J. C.; Soria, J. *J. Catal.* **2000**, 190, 387. (c) Graham, G. W.; Jen, H.-W.; McCabe, R. W.; Straccia, A. M.; Haack, L. P. *Catal. Lett.* **2000**, 67, 99.
- (5) (a) Trovarelli, A. *Catal. Rev. Sci. Eng.* **1996**, 38, 439. (b) Kašpar, J.; Fornasiero, P.; Graziani, M. *Catal. Today* **1999**, 50, 285.
- (6) Liu, G.; Rodriguez, J. A.; Hrbek, J.; Dvorak, J.; Peden, C. H. F. *J. Phys. Chem. B* **2001**, 105, 7762.
- (7) Sayle, T. X. T.; Parker, S. C.; Catlow, C. R. A. *Surf. Sci.* **1994**, 316, 329.
- (8) Stubenrauch, J.; Vohs, J. M. *J. Catal.* **1996**, 159, 50.
- (9) Cordatos, H.; Ford, D.; Gorte, R. J. *Phys. Chem.* **1996**, 100, 18128.
- (10) (a) Mamontov, E.; Egami, T.; Brezny, R.; Koranne, M.; Tyagi, S. *J. Phys. Chem. B* **2000**, 104, 11110. (b) Mamontov, E.; Egami, T. *J. Phys. Chem. Sol.* **2000**, 61, 1345.
- (11) (a) de Carolis, S.; Pascual, J. L.; Petterson, L. G. M.; Baudin, M.; Wojcik, M.; Hermansson, K.; Palmqvist, A. E. C.; Muhammed, M. *J. Phys. Chem. B* **1999**, 103, 7627. (b) Balducci, G.; Islam, M.; Kašpar, J.; Fornasiero, P.; Graziani, M. *Chem. Mat.* **2000**, 12, 677. (c) Liu, W.; Wadia, C.; Flytzani-Stephanopoulos, M. *Catal. Today* **1996**, 28, 391.
- (12) Rodriguez, J. A. *Theor. Chem. Acc.* **2002**, 107, 117.
- (13) Putna, E. S.; Bunluesin, T.; Fan, X. L.; Gorte, R. J.; Vohs, J. M.; Lakis, R. E.; Egami, T. *Catal. Today* **1999**, 50, 343.
- (14) (a) Fornasiero, P.; Fonda, E.; Di Monte, R.; Vlaic, G.; Kašpar, J.; Graziani, M. *J. Catal.* **1999**, 187, 177. (b) Rossignol, S.; Madier, Y.; Duprez, D. *Catal. Today* **1999**, 50, 261.
- (15) Martínez-Arias, A.; Fernández-García, M.; Ballesteros, V.; Salamanca, L. N.; Conesa, J. C.; Otero, C.; Soria, J. *Langmuir* **1999**, 15, 4796.
- (16) Gennard, S.; Corà, F.; Catlow, C. R. A. *J. Phys. Chem. B* **1999**, 103, 10158.
- (17) Fernández-García, M.; Martínez-Arias, A.; Hungria, A. B.; Iglesias-Juez, A.; Conesa, J. C.; Soria, J. *Phys. Chem. Chem. Phys.* **2002**, 4, 2473.
- (18) Zhang, F.; Chan, S.-W.; Spanier, J. E.; Apak, E.; Jin, Q.; Robinson, R. D.; Herman, I. P. *Appl. Phys. Lett.* **2002**, 80, 127.
- (19) Martínez-Arias, A.; Fernández-García, M.; Hungria, A. B.; Conesa, J. C.; Munuera, G. *J. Phys. Chem. B*, in press.
- (20) (a) Fally, F.; Perrichon, V.; Vidal, H.; Kaspar, J.; Blanco, G.; Pintado, J. M.; Bernal, S.; Colon, G.; Daturi, H.; Lavalley, J. C. *Catal. Today* **2000**, 59, 373. (b) Nagai, Y.; Yamamoto, T.; Tanaka, T.; Yoshida, S.; Nonaka, T.; Okamoto, T.; Suda, A.; Sugiura, M. *Catal. Today* **2002**, 74, 225.
- (21) (a) Norby, P.; Hanson, J. *Catal. Today* **1998**, 39, 301 and references therein. (b) Rodriguez, J. A.; Hanson, J. C.; Chaturvedi, S.; Maiti, A.; Brito, J. L. *J. Chem. Phys.* **2000**, 112, 935.
- (22) Chen, J. G. *Surf. Sci. Rep.* **1997**, 30, 1.
- (23) Fernández-García, M. *Catal. Rev.-Sci. Eng.* **2002**, 44, 59.
- (24) Payne, M. C.; Allan, D. C.; Arias, T. A.; Johannopoulos, J. D. *Rev. Mod. Phys.* **1992**, 64, 1045.
- (25) Sohlberg, K.; Pantelides, S. K.; Pennycook, S. J. *J. Am. Chem. Soc.* **2001**, 123, 6609 and references therein.
- (26) (a) Fierro, J. L. G.; Soria, J.; Sanz, J.; Rojo, J. M. *J. Solid State Chem.* **1987**, 66, 154. (b) Fierro, J. L. G.; Mendioroz, S.; Oliván, A. *J. Colloid Interface Sci.* **1985**, 107, 60.
- (27) (a) Bruce, L. A.; Hoang, M.; Hoang, M.; Hughes, A. E.; Turney, T. W. *App. Catal. A* **1996**, 134, 351. (b) Lamonier, C.; Ponchel, A.; D'Huysser A.; Jalowiecki-Duhamel, L. *Catal. Today* **1999**, 50, 247.
- (28) Hastings, J. B.; Suortii, P.; Thomsolin, P.; Kvick, A.; Koetzle, T. *Nucl. Instrum. Methods* **1983**, 208, 55.
- (29) Chupas, P. J.; Cirraolo, M. F.; Hanson, J. C.; Grey, C. P. *J. Am. Chem. Soc.* **2001**, 123, 1694.
- (30) Clausen, B. S.; Steffensen, G.; Fabius, B.; Villadsen, J.; Freidenhans, R.; Topsøe, H. *J. Catal.* **1991**, 132, 524.
- (31) Hammersely, A. P.; Svensson, S. O.; Thompson, A. *Nucl. Instrum. Methods Phys. Res.* **1994**, 346, 321.
- (32) Larson, A. C.; von Dreele, R. B. GSAS General Structure Analysis System. Report LAUR 86-748; Los Alamos National Laboratory: Los Alamos, NM, 1995.
- (33) Norby, P.; Pashni, F. I.; Gualtieri, A. F.; Hanson, J. C.; Grey, C. P. *J. Phys. Chem. B* **1998**, 102, 839.
- (34) Rodriguez, J. A.; Hanson, J. C.; Chaturvedi, S.; Maiti, A.; Brito, J. L. *J. Phys. Chem. B* **2000**, 104, 8145.
- (35) Milman, V.; Winkler, B.; White, J. A.; Pickard, C. J.; Payne, M. C.; Akhmatkaya, E. V.; Nobes, R. H. *Int. J. Quantum Chem.* **2000**, 77, 895.
- (36) Rodriguez, J. A.; Jirsak, T.; Sambasivan, S.; Fischer, D.; Maiti, A. *J. Chem. Phys.* **2000**, 112, 9929.
- (37) (a) Sorescu, D. C.; Rusu, C. N.; Yates, J. T. *J. Phys. Chem. B* **2000**, 104, 4408. (b) Sorescu, D. C.; Yates, J. T. *J. Phys. Chem. B* **1998**, 102, 4556.
- (38) Rodriguez, J. A.; Maiti, A. *J. Phys. Chem. B* **2000**, 104, 3630.
- (39) Refson, K.; Wogelius, R. A.; Fraser, D. G.; Payne, M. C.; Lee, M. H.; Milman, V. *Phys. Rev. B* **1995**, 52, 10823.
- (40) Rodriguez, J. A.; Jirsak, T.; Pérez, M.; Chaturvedi, S.; Kuhn, M.; González, L.; Maiti, A. *J. Am. Chem. Soc.* **2000**, 122, 12362.
- (41) Vanderbilt, D. *Phys. Rev. B* **1990**, 41, 7892.
- (42) Monkhorst, H. J.; Pack, J. D. *Phys. Rev. B* **1976**, 13, 5188.
- (43) Perdew, J. P.; Burke, K.; Ernzerhof, M. *Phys. Rev. Lett.* **1996**, 77, 3865.
- (44) Segall, M. D.; Pickard, C. J.; Shah, R.; Payne, M. C. *Phys. Rev. B* **1996**, 54, 16317.
- (45) Segall, M. D.; Pickard, C. J.; Shah, R.; Payne, M. C. *Mol. Phys.* **1996**, 89, 571.
- (46) (a) Szabo, A.; Ostlund, N. S. *Modern Quantum Chemistry*; McGraw-Hill: New York, 1989. (b) Wiberg, K. B.; Rablen, P. R. *J. Comput. Chem.* **1993**, 14, 1504.

- (47) (a) Calculated using the REFLEX program [47b, c]. (b) Scherrer, P. *Gott. Nachr.* **1918**, 2, 98. (c) Young, R. A. *The Rietveld Method*; IUCr Monographies of Crystallography 5; Oxford University Press: Oxford, U.K., 1995.
- (48) Vlaic, G.; Di Monte, R.; Fornasiero, P.; Fonda, E.; Kašpar, J.; Graziani, M. *J. Catal.* **1999**, 182, 378.
- (49) Kittel, C. *Introduction to Solid State Physics*, 6th ed.; Wiley: New York, 1986; p 76.
- (50) El Fallah, J.; Boujana, S.; Dexpert, H.; Kiennemann, A.; Majerus, J.; Touret, O.; Villain, F.; Le Normand, F. *J. Phys. Chem.* **1994**, 98, 5522.
- (51) Christensen, A.; Carter, E. A. *Phys. Rev. B* **1998**, 58, 8050.
- (52) Thromat, N.; Noguera, C.; Gautier, M.; Jollet, F.; Duraud, J. P. *Phys. Rev. B* **1991**, 44, 7904.
- (53) Mullins, D. R.; Overbury, S. H.; Huntley, S. H. *Surf. Sci.* **1998**, 409, 307.
- (54) Wuilloud, E.; Delley, B.; Schneider, W.-D.; Baer, Y. *Phys. Rev. Lett.* **1984**, 53, 202.
- (55) Koelling, D. D.; Boring, A. M.; Wood, J. H. *Solid State Commun.* **1983**, 47, 227.
- (56) (a) Orlando, R.; Pisani, C.; Roetti, C.; Stefanovich, E. *Phys. Rev. B*, **1992**, 45, 592. (b) Guittet, M. J.; Crocombette, J. P.; Gautier-Soyer, M. *Phys. Rev. B* **2001**, 63, 125 117.
- (57) Kung, H. H. *Transition Metal Oxides: Surface Chemistry and Catalysis*; Elsevier: New York, 1989.
- (58) Overbury, S. H.; Huntley, D. R.; Mullins, R. F.; Cleave, G. N. *Catal. Lett.* **1998**, 51, 133 and references therein.
- (59) Ray, S. P.; Cox, D. E. *J. Solid State Chem.* **1975**, 15, 333.
- (60) Baernighausen, H.; Schiller, G. *J. Less Common Met.* **1985**, 110, 385.
- (61) (a) Daturi, M.; Finocchio, E.; Binet, C.; Lavalley, J. C.; Fally, F.; Perrichon, V.; Vidal, H.; Hickey, N.; Kašpar, J. *J. Phys. Chem. B* **2000**, 104, 9186. Fornasiero, P.; Di Monte, R.; Rao, G.; Kašpar, J.; Meriani, S.; Trovarelli, A.; Graziani, M. *J. Catal.* **1995**, 151, 168.
- (62) Balducci, G.; Kašpar, J.; Fornasiero, P.; Granziani, M.; Islam, M. S.; Gale, J. D. *J. Phys. Chem. B* **1997**, 101, 1750.